Ceramics



Superstructure reflections in 40% Sn(II)-substituted BaZr_{0.5}Ti_{0.5}O₃ perovskite modeled with a Bayesian method for crystallographic refinement

Rachel Broughton^{1,*}, Shaun O'Donnell², Eric Gabilondo², Ryan Newell¹, Paul A. Maggard², and Jacob L. Jones^{1,*}

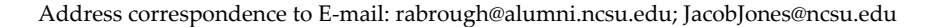
Received: 22 April 2024 Accepted: 6 June 2024 Published online: 20 June 2024

© The Author(s), under exclusive licence to Springer Science+Business Media, LLC, part of Springer Nature, 2024

ABSTRACT

Tin(II) perovskite oxides are promising for lead-free ferroelectric applications because Sn(II) is isoelectronic to Pb(II) and is predicted to amplify displacements and polarization. Though typically difficult to synthesize, a metastable perovskite structure of barium zirconate titanate with Sn(II) substituted for Ba was recently reported. In the present work, a detailed structural analysis is performed on 40% Sn(II)-substituted BaZr_{0.5}Ti_{0.5}O₃ with high-resolution synchrotron X-ray diffraction. The main diffraction peaks of the cubic perovskite persist with the incorporation of tin into the structure. Additionally, superstructure reflections are observed in the low 2θ region of the diffraction pattern at d-spacings that are multiples of the main perovskite peaks. The origin of these superstructure peaks is attributed to atomic displacements of the Sn and Zr/Ti cations. A Bayesian inference method is applied to conduct a refinement of the atomic displacements in a supercell with no symmetry constraints (i.e., P1 symmetry setting) using the superstructure diffraction reflections. In the absence of a known structure and symmetry, the Bayesian method allows for simultaneous refinement of all atomic positions without convergence to unrealistic local minima, resulting in the most probable configurations of atoms. Through the refined solution, it is found that displacements of the cations result in symmetry-breaking distortions from the parent cubic perovskite structure that can be modeled using a P1 supercell with the potential for ferroelectric polarization.

Handling Editor: M. Grant Norton.





¹ Department of Materials Science and Engineering, North Carolina State University, Raleigh, NC 27695, USA

² Department of Chemistry, North Carolina State University, Raleigh, NC 27695, USA

Data 99% Credible Interval 99% Prediction Interval 99% Prediction Interval 2 4 6 8 10 12 14 16 18 20 22 24 29 (°)

GRAPHICAL ABSTRACT

Introduction

Perovskite oxides with the formula ABO₃, where A and B are metal cations, are widely used in electronic applications due to their attractive dielectric, piezoelectric, and ferroelectric properties. Perovskites with Pb²⁺ on the A-site, such as PbTiO₃ and Pb(Zr,Ti)O₃, are ubiquitously used because of their superior properties relative to other compositions. However, finding alternatives to Pb-based perovskites is important as there are known health risks associated with the manufacture of Pb-based perovskites and concerns over disposal of the product at its end of life [1, 2].

Perovskites with Sn²⁺ on the A-site are compounds of technological interest because of their potential to exhibit ferroelectric properties comparable or superior to the Pb-based compounds. First principles calculation studies predict that SnTiO₃ and SnZr_{0.5}Ti_{0.5}O₃ would exhibit a perovskite structure with a tetragonal distortion analogous to their Pb equivalents [3, 4]. For epitaxial thin films, first principles calculations by Pitike et al. predict that SnTiO₃ would undergo a transition from a tetragonal P4mm phase to a monoclinic Cm phase under biaxial tension [5]. In one experimental study, Laurita et al. found that the presence of a small amount of Sn²⁺ dopant in $Ba_{0.79}Ca_{0.16}Sn_{0.05}TiO_3$ and $Sr_{0.9}Sn_{0.1}TiO_3$ influenced the local structure of the compounds to be similar to that of PbTiO₃ [6]. However, Sn(II)-containing perovskites have repeatedly proved difficult to synthesize [7]. The complexity of synthesis has limited experimental studies of such Sn(II)-containing compositions and, specifically, their structures and the behavior of the Sn²⁺ cations.

Recently, the ability to substitute $\rm Sn^{2+}$ on the A-site of $\rm ABO_3$ perovskite oxides to form metastable $\rm Sn(II)$ -substituted $\rm Ba(Zr,Ti)O_3$ and $\rm BaHfO_3$ compounds was demonstrated by O'Donnell et al. and Gabilondo et al. [8–10]. The synthesis was achieved with a novel application of a molten salt flux exchange method, which enables the experimental investigation of structures of $\rm Sn(II)$ -substituted perovskites. In the present work, the structure of $\rm 40\%~Sn(II)$ -substituted $\rm BaZr_{0.5}Ti_{0.5}O_3$ is studied via high-resolution synchrotron X-ray diffraction (XRD). In contrast with the predicted tetragonal structure, a perovskite structure with cubic cell metrics and superstructure reflections is observed in the XRD pattern.

Perovskites are known to exhibit small, yet transformational, changes in their crystal structures with small changes in stoichiometry, temperature, etc. Studies have shown that perovskites undergo octahedral tilting, cation displacements, and distortions, especially when the structures are intermediate or frustrated [11, 12]. These displacive variations often give rise to extra reflections, sometimes termed superstructure reflections, that can be observed with X-ray, neutron, or electron diffraction techniques [13]. In the work described herein, the presence of the observed superstructure reflections is attributed to distortions, specifically as a result of the Sn²⁺ and Zr⁴⁺/Ti⁴⁺ cation displacements. Since no known perovskite crystal



structure could account for all superstructure reflections, the atomic displacements were modeled using a supercell approach with a Bayesian inference method for crystallographic refinement to determine the most probable configuration of atoms. The Bayesian method provides an alternative minimization routine to the traditional Rietveld method for refinement of a large supercell with atoms free to displace in all directions with no pre-defined symmetry [14, 15]. With this approach, a most probable supercell of the tinrich perovskite phase is determined that captures the behavior of all the observed superstructure reflections. The cation displacement behavior in the lattice of the Bayesian structural solution is examined, and the distortion modes relating the parent cubic structure to the supercell are analyzed. Within the solved structure, a potential symmetry-breaking distortion mode indicating the possibility for ferroelectric behavior was identified.

Methods

Synthesis

The powders $BaZr_{0.5}Ti_{0.5}O_3$ (BZT) and 40% Sn(II)-substituted $Ba_{0.6}Sn_{0.4}Zr_{0.5}Ti_{0.5}O_3$ (BSZT) were prepared in the same way as previously described by O'Donnell et al. [8, 16]. In summary, the precursor BZT was first prepared through a flux synthesis procedure by combining $BaCO_3$ (Alfa Aesar, 99.8%), TiO_2 (J.T. Baker, > 99%), and ZrO_2 (Beantown Chemical, 99.5%). The Sn(II) A-site substitution was performed through a flux-assisted synthesis with $SnCl_2$ (Alfa Aesar, 99% min) and SnF_2 (Alfa Aesar, 97.5%) under an inert argon atmosphere.

Characterization

High-resolution synchrotron powder XRD data were measured on beamline 11-BM at the Advanced Photon Source (APS), Argonne National Laboratory. An average wavelength of 0.457929 Å was used, and scans were collected over a 2θ range of 0.5° – 50° with a step size of 0.001° at room temperature.

XRD patterns were measured at high temperatures, in situ, at beamline 11-ID-C at the APS. The powder sample was prepared and sealed in a fused silica capillary in a glovebox under an argon atmosphere. A hot air blower was used to heat the sample from room

temperature to 800 °C at a rate of 5 °C/min. The sample was held for 2 h at 800 °C and then cooled back to room temperature at a rate of 5 °C/min. During heating and cooling, two-dimensional diffraction patterns were collected on an area detector every 60 s using an average wavelength of 0.1173 Å (equating to a 106 keV energy) over a 2θ range of 0.5°–15°. The area diffraction images were integrated to line diffraction patterns using the program GSAS-II (General Structure Analysis System 2) and a LaB₆ standard for calibration of the sample-to-detector distance [17].

Analysis

Phase identification was performed through the program High Score plus by using the Search & Match function with the International Centre for Diffraction Data (ICDD) Powder Diffraction File database (PDF-4+) [18].

Cubic perovskite structures of the BZT and the BSZT were refined using the Rietveld method with the high-resolution synchrotron data in the GSAS-II program [17]. Three refinements with the Rietveld method were conducted in this work: one on the BZT data with a Pm3m BZT phase, one on the BSZT data with a single *Pm3m* BSZT phase, and one on the BSZT data with a two-phase model consisting of Sn-rich and Ba-rich distinct Pm3m phases. Generally, all refinements were performed in the following parameter turn-on sequence: background, histogram scale, lattice parameters, sample *x*-displacement, microstrain, size, sample absorption, atomic displacement parameters (U_{iso}) , atomic occupancy fractions, and phase fractions. Phase fraction is defined by the fraction of unit cells of each constituent. Parameters were sequentially refined one at a time while turning all other parameters off. Then, stable parameters were co-refined simultaneously while less-stable parameters were fixed until a reasonable result was achieved. The Zr/Ti (B-site) $U_{\rm iso}$ values were constrained to be equal, and the total B-site occupancy fraction was constrained to sum to one in all refinements. Analogous constraints for the Ba/Sn on the A-site were applied for the one-phase BSZT refinement. The phase fractions of analyte and impurity phases in all refinements were constrained to sum to one.

A Bayesian inference method for crystallographic structure refinement of atomic positions in a supercell was developed and applied to the BSZT high-resolution synchrotron data [14, 15]. The Bayesian



approach differs from the Rietveld method in several important ways: (i) it is formulated using Bayesian inference instead of a least-squares frequentist-based approach, (ii) it employs sampling methods that are more robust against local minima parameter sets, (iii) it provides improved uncertainty quantification, and (iv) it offers a more intuitive understanding of the results while incorporating scientifically informed hypotheses as the posterior distribution functions describe the probabilities of the parameters given prior information. The Bayesian approach for crystallographic refinement was implemented in Python with the package Quantitative Uncertainty Analysis for Diffraction which interfaces with the diffraction model embedded in the GSAS-II program and is publicly available on GitHub [19]. A delayed rejection adaptive metropolis (DRAM) sampling algorithm was used to perform the analysis which was run for 200,000 iterations with 100,000 burn-in, an adaption interval of 100, and a shrinkage of 0.1 for each refinement [14, 20]. For each Bayesian refinement, three independent chains with different initial parameter values were run simultaneously to evaluate convergence behavior by comparing the trace plots and mean solutions of the three individual runs. Initial parameters were taken as the nondisplaced original atomic positions in (x, y, z)fractional coordinates, original positions plus 0.001 Å, and original positions minus 0.001 Å. The results of the 'chain 1' runs with initial parameters of the nondisplaced atomic positions are presented in the main text unless otherwise noted.

Results

Phase identification in high-resolution powder X-ray diffraction profiles

High-resolution synchrotron XRD measurements of BZT and Sn(II)-substituted BSZT are presented in Fig. 1. The pattern of the precursor BZT material, plotted at the bottom, shows the characteristic peaks of a cubic perovskite structure, space group No. $221 \, Pm\overline{3}m$. There is a small amount of impurity ZrO_2 baddeleyite phase, space group No. $14 \, P2_1/c$. Additionally, a cubic perovskite BaZrO₃ impurity phase was observed via diffraction peaks present as shoulders on the main perovskite peaks.

The structural effects of the Sn(II) substitution can be studied through the BSZT high-resolution XRD

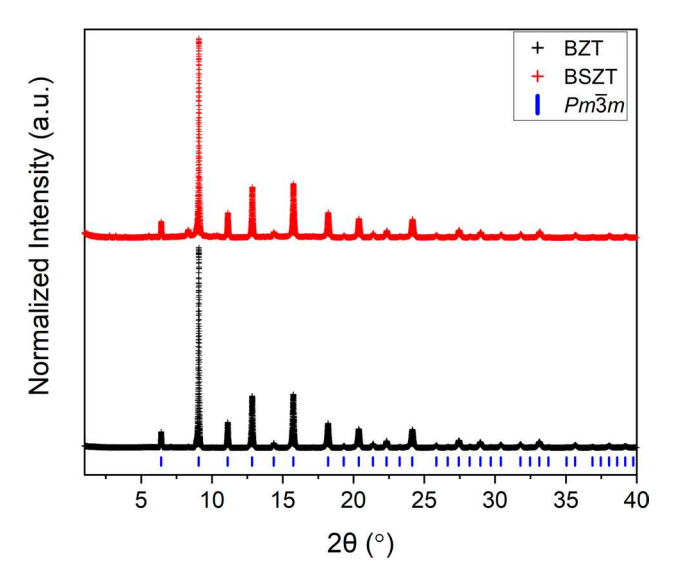


Figure 1 High-resolution synchrotron XRD patterns of BZT (bottom, black) and 40% Sn(II)-substituted BSZT (top, red). The main peaks observed in both compositions are characteristic of a cubic perovskite (space group $Pm\overline{3}m$).

pattern, which is plotted at the top in Fig. 1. The main peaks observed in the BSZT pattern are also characteristic of a cubic perovskite Pm3m structure, at least as observed by the lack of peak splitting which would otherwise indicate a lower symmetry polymorph. The presence of cubic peaks indicates that the structure of precursor BZT perovskite phase persists even with the 40% tin substitution, as discussed previously by O'Donnell et al. [8]. Peaks from the secondary phases present in the precursor remain in the pattern, still in minor fractions. A small amount of SnO, space group No. 129 P4/nmm, is seen by a small peak at around 2θ of 8.78° (equivalent to an interplanar spacing of 2.99 Å) which corresponds with the most intense expected SnO peak. SnO is a decomposition product of metastable Sn(II)-containing perovskite phases [16]; thus, the low presence of SnO in the diffraction pattern indicates that negligible decomposition has occurred within the sample. The phase and weight fractions of all secondary phases present in the pattern obtained through Rietveld refinements are reported later in the text (see Table 2).

In the diffraction pattern of the BSZT, unexpected peaks at low intensities relative to the cubic perovskite reflections are also apparent. Figure 2 highlights the presence of these additional diffraction peaks, marked with asterisks, which are most prominently



Table 1 Observed superstructure reflection positions

	^
d-spacing (Å)	cubic perovskite reflection relationship
11.67	$4 \cdot d_{110}$
9.48	$4 \cdot d_{111}$
8.2	$4 \cdot d_{200}$
6.69	$4 \cdot d_{211}$
5.45	$4 \cdot d_{221}, 4 \cdot d_{300}$
5.23	none
4.94	$4 \cdot d_{311}$
4.73	$4\cdot d_{222}$
4.38	$4 \cdot d_{320}$
3.34	$4 \cdot d_{422}$
3.21	$4 \cdot d_{431}, 4 \cdot d_{510}$
3.15	$4 \cdot d_{333}, 4 \cdot d_{511}$
2.77	$4 \cdot d_{531}$
2.73	$4 \cdot d_{442}, 4 \cdot d_{600}$

Reflection positions are listed as interplanar d-spacing values in the first column. The second column lists the relationships of the d-spacing values to those of the cubic $Pm\bar{3}m$ reflections as multiples of 4. Three of the superstructure reflections correspond to multiples of the cubic unit cell lattice constant (a_c) , listed in the third column

observed near the background intensity level. These unidentified peaks are particularly prominent in the low 2θ region from 2 to 10° as shown in Fig. 2b and remain visible in the pattern at 2θ angles up to ~ 18° , but are not present in the BZT precursor as shown in Fig. 2a. In Table 1, the approximate d-spacing values, or interplanar spacing values, corresponding to the observed unidentified reflections are tabulated along with their relationships to the cubic perovskite unit cell reflections. Notably, most of the d-spacings of the unidentified peaks are multiples of the d-spacings of the main perovskite peaks by a factor of four. After a thorough phase identification procedure was performed, it was found that the additional diffraction peaks can neither be attributed to relevant secondary phases, such as ZrO₂, BaZrO₃, or SnO, nor any other existing perovskite phases in the database. Perovskites distorted by the presence of oxygen octahedral distortions and tilting or cation displacements are known to exhibit extra satellite reflections in diffraction measurements called superstructure reflections [11, 12]. Therefore, the unexpected peaks in the BSZT diffraction pattern are identified as superstructure reflections that are indicative of distortions of the pre-existing perovskite lattice.

Known distorted perovskite structures from literature were examined and are discussed here in an attempt to identify a match, or approximate match, to describe the experimental pattern with a focus on accounting for the BSZT superstructure reflections. Configurations were sought with a unit cell and symmetry that incorporated a quadrupling of the cubic perovskite unit cell in at least one direction to match the reflection positions (Table 1). One example of such a distorted structure is PbZrO₃, which is an orthorhombic structure in the Pbam space group with lattice parameters $\sqrt{2a_c} \times 2\sqrt{2a_c} \times 2a_c$ where a_c denotes the parent cubic perovskite lattice parameter [21-24]. The structural distortions include displacements of the Pb ions and octahedral tilting [25]. Many distorted perovskite variations are similar to the PbZrO₃ structure and generally share common elements. For example, Nd-substituted BiFeO₃ also exhibits superstructure peaks, as studied by Karimi et al. and Levin et al. through diffraction [26, 27]. For Nd-modified compositions, e.g., $Bi_{1-x}Nd_xFeO_3$ with $0.15 \le x \le 0.20$, superlattice peaks were observed and consistent with orthorhombic PbZrO₃ and *Pbam* symmetry. They also observed additional superlattice peaks in the system at $\frac{1}{4}\{00l\}_c$, indicating a quadrupling of the *c*-axis of the original cubic unit cell with lattice parameters $\sqrt{2a_c} \times 2\sqrt{2a_c} \times 4a_c$. A hypothesis presented by Levin et al. to explain the quadrupled structure in Bi_{1-x}Nd_xFeO₃ is an NaNbO₃-type octahedra tilting combined with Bi antipolar displacements with Pbnm symmetry [27, 28]. Likewise, NaNbO₃ is a distorted perovskite with an orthorhombic unit cell in space group *Pbma* with lattice parameters $\sqrt{2a_c} \times 4a_c \times \sqrt{2a_c}$ [29]. Structural refinements of single-crystal XRD and neutron diffraction determined that there are displacements of Na, displacements of Nb, and octahedral tilting within the NaNbO₃ at room temperature [29, 30]. Khalyavin et al. studied the structural distortions of the high-pressure stabilized perovskite system $BiFe_{1-x}Sc_xO_3$ using neutron and x-ray powder diffraction [31, 32]. A BiFe_{0.7}Sc_{0.3}O₃ composition was found to have a *Pnma* space group with cell metrics of $\sqrt{2}a_c \times 4a_c \times 2\sqrt{2}a_c$, Bi displacements, and unusual octahedral tilting. Similarly, BiScO₃ was also found to have a *Pnma* space group, but with $2\sqrt{2}a_c \times 4a_c \times \sqrt{2}a_c$ cell metrics and different structural distortions. While there were some similarities between the structures described above and the BSZT superstructure reflections observed in the work presented here, not all



of the reflections were captured with any one given structure and, additionally, the predicted reflections that did match some of the observed reflections did not well represent their observed intensities.

In situ high-temperature XRD decomposition experiment

The superstructure reflections were studied through an in situ high-temperature XRD experiment to observe the thermal decomposition of the BSZT phase. Area detector patterns, later integrated to line scans, were acquired as the sample was heated from room temperature to 800 °C, held at 800 °C, and cooled back to room temperature. The in situ diffraction patterns for all patterns measured during the heating segment are plotted in Fig. 3 with reflection intensity as the z-scale colormap. In the initial pattern at the start of the experiment, both the primary diffraction reflections evidencing cubic cell metrics and the superstructure reflections are consistent with that observed in the high-resolution XRD data (Figs. 1 and 2). The decomposition of the BSZT, which occurs as the sample is heated and Sn(II) leaves the perovskite lattice, is indicated by the emergence of SnO₂ [33] in the pattern at around 550 °C. The full 2θ range is plotted in supplemental Fig. S1 for a more complete observation of the SnO₂ reflections. The superstructure reflections gradually disappear during the decomposition of the BSZT compound into BZT and SnO₂ and are no longer observable in the pattern after around 600 °C, which is evident when the pattern is examined in the low 2θ region (Fig. 3).

During cooling, the BZT and SnO₂ phases remain prominent, but the superstructure peaks do not return, i.e., displaying irreversibility, as seen in supplemental Fig. S2. The irreversibility of the superstructure reflections upon cooling suggests that they are unique to the metastable tin-containing phase present at the beginning of the experiment.

Tolerance factor considerations

The Goldschmidt tolerance factor is often calculated for perovskites to predict the expected stability and oxygen octahedral tilting in the structure at room temperature [13]. The tolerance factor, *t*, is defined as

$$t = \frac{(r_A + r_O)}{\sqrt{2}(r_B + r_O)},$$

where r_A , r_B , and r_O are the ionic radii of the A-site atoms, B-site atoms, and oxygen atoms, respectively. The B-site atoms are classified as those in the center of the oxygen octahedra. Shannon's ionic radii of the respective atoms, as listed in Table S1, were used for the tolerance factor calculation [34, 35]. The ionic radius of $\rm Sn^{2+}$ was not reported in Shannon's original tables because of the asymmetric bond distances from distortion. Recently, the ionic radius of $\rm Sn^{2+}$ was derived using methods analogous to the Shannon radii system by Sidey as 1.38 Å in 12-fold coordination [36], a value that is adopted here in the tolerance factor calculations.

The Goldschmidt tolerance factor of BZT is t = 1.03, and that of SnZr_{0.5}Ti_{0.5}O₃ (SZT) with Sn²⁺ fully occupying the A-site is t = 0.95. When the tolerance factor is in the range 0.985 < t < 1.06, the perovskite is expected to be untilted and undistorted, whereas when 0.71 < t < 0.964, the perovskite is expected to exhibit both antiphase and in-phase octahedral tilting [13]. The tolerance factor of BZT, t = 1.03, is in the range to expect an undistorted, untilted cubic perovskite structure. SZT, on the other hand, with a tolerance factor of t = 0.95, may be susceptible to tilting or other distortions to stabilize the structure, which is consistent with the appearance of superstructure peaks in the XRD profile. For a mixed A-site Ba_{0.6}Sn_{0.4}Zr_{0.5}Ti_{0.5}O₃, the stoichiometrically average value is t = 1.0, which suggests an undistorted perovskite. However, Ba-rich and Sn-rich zirconate titanate phases in BSZT were shown in prior work to form separately within the system as a core and nanoshell configuration [16]. The observation of superstructure reflections in the BSZT diffraction pattern is consistent with the presence of Sn-rich regions that would have a tolerance factor closer to t = 0.95.

Refinements with the Rietveld method and structure determination

Structural refinements using the Rietveld method of the BZT and BSZT samples were performed with the high-resolution XRD data over a 2θ range of 2–45°. Both patterns were fit using a one-phase model with a single cubic perovskite ($Pm\bar{3}m$) phase as well as the identified impurity phases, but the superstructure



Table 2 Refinement results from the Rietveld method for parameters of most interest for BZT, BSZT with a one-phase model, and BSZT with a two-phase BZT+SZT model

Parameter name	Value	s.u
BZT		
Lattice parameter (Å)	4.09585	0.00004
Zr fraction	0.429	0.003
BZT phase fraction	0.97	*
BaZrO ₃ phase fraction	0.02	*
ZrO ₂ phase fraction	0.01	*
$R_{\rm wp}$ (%)	16.92	
BSZT 1-phase		
Lattice parameter (Å)	4.09306	0.00003
Sn fraction	0.349	0.004
Zr fraction	0.413	0.003
BSZT phase fraction	0.952	*
BaZrO ₃ phase fraction	0.018	*
ZrO ₂ phase fraction	0.025	*
SnO phase fraction	0.005	*
R_{wp} (%)	11.10	
BSZT 2-phase		
BZT		·
Lattice parameter (Å)	4.09596	0.00005
Zr fraction	0.575	0.006
BZT phase fraction	0.607	0.007
SZT		
Lattice parameter (Å)	4.08643	0.0000
Zr fraction	0.110	0.008
SZT phase fraction	0.345	0.006
Impurities		
BaZrO ₃ phase fraction	0.018	*
ZrO ₂ phase fraction	0.025	*
SnO phase fraction	0.005	*
R_{wp} (%)	10.07	

Refined parameter values and associated standard uncertainties (s.u.) are listed with weighted pattern residual R-values ($R_{\rm wp}$). Parameter values that were refined individually, but fixed for the final refinement as they were not stable enough to be co-refined are marked with asterisks (*)

reflections were initially ignored for a simplified refinement of only the parent cubic structure. In addition to the one-phase model, the BSZT pattern was also fit with a two-phase model with separate cubic BZT and SZT phases. This two-phase model was inspired by previously published TEM images that showed the Sn-rich perovskite phase forms a shell around a Ba-rich circular perovskite core, suggesting that the SZT is stabilized on the surface of the BZT as a separate phase [16]. The refined parameter values and

criteria of fit results for all refinements are reported in Table 2. The two-phase BZT + SZT model resulted in the best fit to the BSZT data, and the refinement results are presented in Fig. 4. Plots of the modeled patterns and observed data for the single-phase BSZT and BZT models are presented in supplemental information Fig. S3. Parameters refined that are not listed in Table 2 include atomic displacement parameters ($U_{\rm iso}$), microstrain, size, histogram scale, sample x-displacement, absorption, and background. The total phase



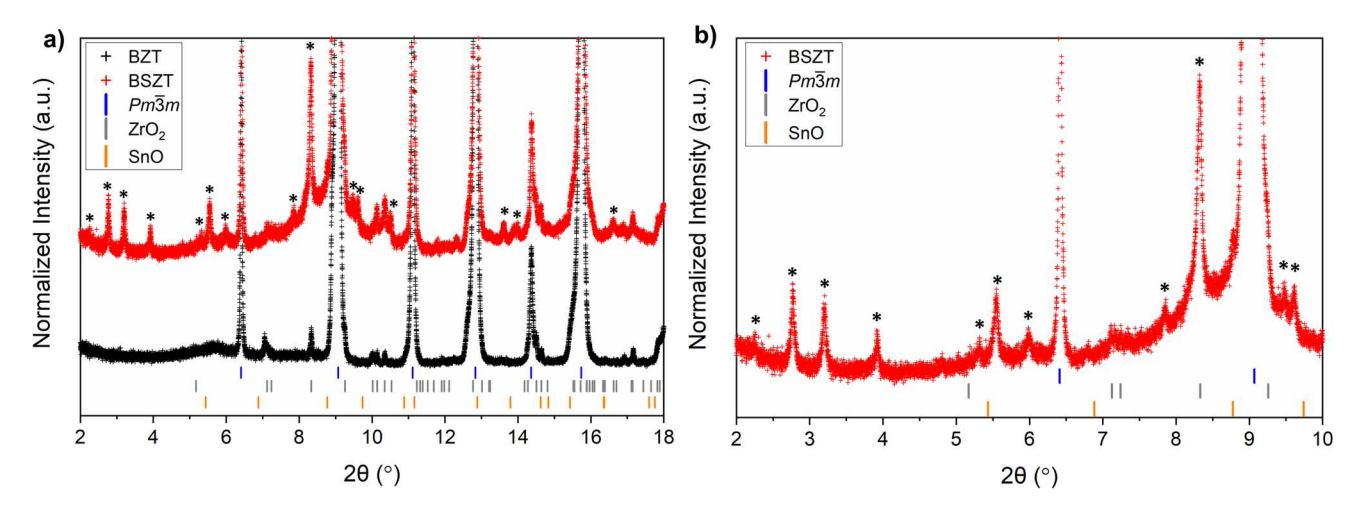


Figure 2 High-resolution XRD viewed near the background intensity level **a** over a 2θ range of 2–18° to highlight the appearance of superstructure reflections that are present in the BSZT (top, red) and not in the precursor BZT (bottom, black). **b** Fur-

ther zoomed in 2θ range of 2–10° to display the most prominent superstructure reflections. Visible superstructure reflections are marked by asterisks (*) and impurity phases $\rm ZrO_2$ and $\rm SnO$ are denoted by colored tick marks.

fraction of all the impurity phases combined is less than 5% in each refinement with a nearly negligible amount of SnO impurity, indicating that only a small amount of decomposition has occurred in the sample. The cubic lattice constant of the single-phase BSZT model $(4.09306 \pm 0.00003 \text{ Å})$ is slightly less than that of the precursor BZT $(4.09585 \pm 0.00004 \text{ Å})$ which is likely due to the smaller size of Sn²⁺ compared to Ba²⁺ (Table S1) and supports the expectation that, on average, Sn²⁺ ions are substituting for Ba²⁺ in the BZT lattice. The two-phase BZT + SZT model has a BZT lattice constant $(4.09596 \pm 0.00005 \text{ Å})$ similar to that of the BZT precursor refinement and an SZT lattice constant $(4.08643 \pm 0.00008 \text{ Å})$ noticeably smaller than the BZT. Additionally, the weighted pattern residual (R_{wp}) of the two-phase BZT + SZT model, 10.074%, is less than that of the one-phase model for BSZT, 11.103%. While this difference in agreement factors is slight, it suggests that the two-phase model provides a more reasonable fit to the experimental data in accordance with the previously observed core–shell microstructure.

While the two-phase model involving two cubic phases provides a good fit to the diffraction data, the superstructure reflections are not predicted from these cubic phases and, therefore, the model needs to be further improved to better understand the structure. However, no known structures were found to adequately account for all the superstructure reflections in the phase identification process. Thus, the pre-existing structural models found in literature are

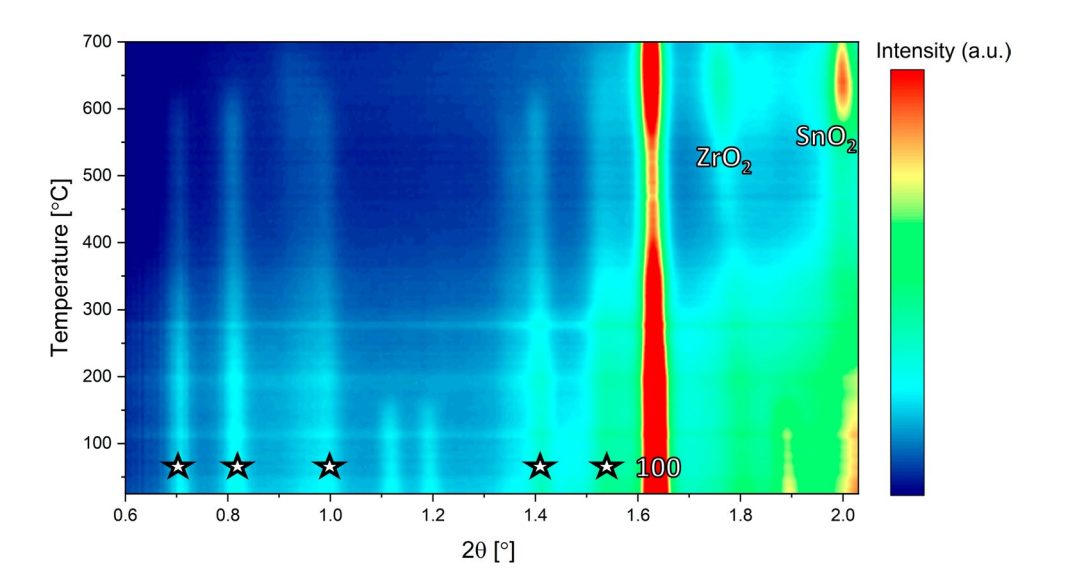
insufficient, so the symmetry must be lowered and the atomic positions must be refined to improve the fit. A structural determination can be performed when no known structure exists, which can sometimes be completed successfully with powder XRD information alone [37]. The program EXPO2014 was used to index the unit cell from the XRD pattern [38]. Though there were several possible results, one of the most likely set of unit cell parameters resulting from this search was a = 16.37 Å, b = 5.87 Å, c = 11.60 Å, $\alpha = \beta = \gamma = 90^{\circ}$. This definition of lattice parameters corresponds to cell metrics of $4a_c$, $\sqrt{2}a_c$, $2\sqrt{2}a_c$, where $a_c \approx 4.1$ Å. The lattice parameter definition agrees with the unit cell dimensions of the PbZrO₃ orthorhombic perovskite structure doubled along one axis [21, 24]. Among other attempted structure determination techniques, space group determination was not possible within EXPO2014 due to the relatively low intensities of the superstructure reflections and peak overlap of the impurity phases, main perovskite BZT reflections, and superstructure reflections. Thus, structure determination was constrained to indexing and determining the most likely set of unit cell dimensions.

Structural investigation with the Bayesian inference method

Given the inability of known phases to fit the observed superstructure reflections and their intensities, an alternative method is presented that can refine the



Figure 3 In situ XRD patterns during decomposition of BSZT in the low 2θ region to examine the most prominent superstructure reflections. Star symbols indicate observed superstructure reflections, and labels indicate the cubic 100 reflection, ZrO₂ impurity and emerging SnO₂ decomposition product. After complete decomposition (around 600 °C), the superstructure reflections are no longer visibly present and do not return upon cooling.



crystal structure and model all superstructure reflections observed in the XRD pattern.

When considering the construction of the new structural model, several possible perovskite distortions that could cause the presence of superstructure reflections are considered including: tilting of the oxygen octahedra, cation ordering, and cation displacements [12]. Several distortion types can be ruled out through process of elimination given that the superstructure reflections are visible by XRD and are commensurate with four times the cubic perovskite unit cell. From the tolerance factor calculations and what we know of perovskite-type structures, tilting of the oxygen octahedra is likely present in the structure. However, XRD is not highly sensitive to oxygen atoms in the presence of heavier elements, so the oxygen tilting pattern cannot be sufficiently determined from this information alone. B-site cation ordering of the zirconium and titanium is also dismissed because, in prior work on an Sn(II)-substituted PbHfO₃ system, similar superstructure reflections were observed with only the Hf occupying the B-site [39]. Additionally, an even distribution of Zr and Ti throughout individual particles of the 40% Sn(II)-substituted BaZr_{0.5}Ti_{0.5}O₃ was observed by energy-dispersive x-ray spectroscopy (EDS) measurements collected via transmission electron microscopy (TEM) methods in a previous study by O'Donnell et al. [16]. A-site cation ordering of the Ba and Sn atoms is also unlikely because, in the same TEM imaging study by O'Donnell et al., it was shown that the BSZT forms in a core-shell structure with a Ba-rich core and a separate Sn-rich shell. Thus, the BZT and SZT are two separate phases that can be modeled independently as opposed to a mixed Ba/Sn A-site, in agreement with the previously discussed Rietveld refinements. After eliminating oxygen behavior and cation ordering, this leaves cation displacements. Furthermore, since Sn²⁺ has a smaller ionic radius than Ba²⁺ and an electron lone pair like Pb²⁺, the Sn²⁺ ions are expected to experience larger displacements, whereas Ba²⁺ is less susceptible to distorting from its centrosymmetric position. Thus, it is hypothesized that the primary contributions to the intensities of the observed XRD superstructure peaks are attributed to cation displacements of the Sn²⁺ and/or the Zr⁴⁺/Ti⁴⁺ B-site cations.

To refine the cation displacements using the powder XRD data, one approach could be to create a supercell based on the cubic perovskite precursor and refine the atomic positions using the Rietveld method. Since the space group is unknown, no symmetry elements could be applied in this approach, allowing atoms to move in any direction. Consequently, when this approach was attempted using the Rietveld method, it led to unstable refinements, poor fits to the superstructure reflections, and unrealistic values for atomic coordinates.

Alternatively, applying a Bayesian inference method to the refinement of the structure can provide a more robust algorithm for testing and accepting atomic positions. With this Bayesian method, all refinement parameters are sampled simultaneously over hundreds of thousands of iterations until a converged solution is obtained. The method results in posterior distributions of solutions for parameter values. Such a probabilistic model can be summarized



by computing the mean values of each posterior distribution. In this work, the mean posterior parameter values for the atomic position parameters are taken to be the 'solved' values that determine the most probable supercell configuration. Additionally, within the Bayesian method, atoms are constrained through prior information to displace only within a defined radius of their nondisplaced positions to avoid false minima and unreasonable solutions.

To implement the Bayesian method, a non-distorted SZT superstructure with cell metrics was first defined. The supercell lattice definition is constructed using a transformation of the parent undistorted perovskite cubic unit cell ($a_c \times a_c \times a_c$) to an orthorhombic setting ($\sqrt{2}a_c \times 2\sqrt{2}a_c \times 4a_c$). The transformation was performed in Crystal Maker [40] as:

$$a_o = a_c + b_c$$

$$b_o = -2a_c + 2b_c$$

$$c_o = 4c_c$$

Here, a_o , b_o , and c_o are the orthorhombic supercell unit cell vectors and $a_{c'}$ $b_{c'}$ and c_c are the cubic perovskite unit cell vectors. The parent cubic unit cell atomic positions were initialized as Sn(0, 0, 0), Ti/Zr(0.5, 0.5, 0.5), and O(0.5, 0.5, 0) and a shift in origin of $(0.5a_c,$ $0b_c$, $0c_c$) was applied for the supercell transformation. This unit cell setting is the same as the PbZrO₃ distorted perovskite definition with the *c*-axis doubled [21, 24]. A space group of P1 was chosen, such that no symmetry was assigned to the supercell. To define the magnitudes of the supercell lattice parameters, a value of $a_c = 4.1$ Å was used, as determined using the Unit Cell Test & Refinement tool in GSAS-II to manually adjust the supercell dimensions until all the expected reflection positions aligned with the visible superstructure peaks [17]. The supercell lattice parameter magnitude ratios were fixed at $\sqrt{2a_c} \times 2\sqrt{2a_c} \times 4a_c$, resulting in dimensions of $5.798 \times 11.596 \times 16.4$ Å. All atomic positions, including those of the oxygen, titanium/zirconium, and tin, were fixed at their nondisplaced positions to define this initial non-distorted structure. The B-site atoms were all defined at 50% Zr and 50% Ti occupancy and constrained to be an equivalent mixed site.

The second step involves performing a refinement with the Rietveld method in GSAS-II in order to initialize the Bayesian crystallographic refinement

algorithm. Here, we assume the two-phase model with separate BZT and SZT phases as discussed in the previous section, where the behavior of the SZT structure is of interest. To set up the Rietveld refinement, solved parameters from the two-phase refinement of the BZT + SZT (Fig. 4 and Table 2) were used as initial parameter settings. The SZT phase with a P1 supercell was used in place of the cubic SZT phase from the two-phase refinement. The weight fractions of the BZT and SZT phases were fixed to 0.6 and 0.4, respectively, based on the stoichiometric values as freeing these parameters created an unstable refinement. Using the complete 2θ range between 2 and 45° , the parameters of microstrain, size, histogram scale, sample displacement, background, and the BZT structural information were refined. The SZT supercell structural information remained fixed during the refinement. All parameters were then fixed except for the background parameters and the 2θ range was constrained to 2–8.75°, which is the region of the most prominent and informative superstructure reflections, and a final refinement iteration was performed. This low 2θ region includes only one of the main perovskite peaks, so that the refinement is predominantly influenced by the superstructure reflections instead of the cubic perovskite. Only the ZrO₂ impurity phase was included in the model as the other impurity phases in the sample do not exhibit reflections in this 2θ region.

With the Rietveld refinement complete, the atomic positions within the SZT supercell are then refined using the Bayesian approach. Two different structural refinements with the Bayesian inference method were performed: (Model 1) varying only the Sn x, y, and z fractional atomic position coordinates and (Model 2) varying both the Sn and Zr/Ti B-site x, y, and z fractional atomic position coordinates. Aside from the atomic positions and background parameters, all other parameters remained fixed at their least-squares estimates during the Bayesian refinement. A beginning set of atomic fractional positions within the supercell initializes the routine for obtaining Bayesian 'chains' of sampled and accepted x, y, and z fractional coordinate values for each refined atom. Three parallel sample chains for each refined *x*, *y*, and *z* parameter were run with different initial values for each chain to evaluate convergence and performance of the model. The initial values were set as the atomic fractional coordinates in (x, y, z)of the non-displaced supercell and ± 0.001 of those non-displaced starting values. The resulting mean



Table 3 Fit criteria for results of Models 1 and 2

	$2^{\circ} \le 2\theta \le 8.75^{\circ}$ DIC	$2^{\circ} \le 2\theta \le 8.75^{\circ}$ $R_{\text{wp}} (\%)$	$2^{\circ} \le 2\theta \le 25^{\circ}$ $R_{\text{wp}} (\%)$
Model 1	59,320	9.92	15.35
Model 2	60,670	9.73	15.68

Fit criteria include deviance information criteria (DIC) from the Bayesian refinement approach and weighted pattern residuals (R_{wp}) from the least-squares approach with the SZT structure definition fixed at the Bayesian solution

atomic coordinates of the three separate chains had different values for each atom, but displayed similar atomic displacement relationships within the supercell. Given the similarities of the three separate results for each model, only results for 'chain 1,' the chain with the non-displaced atomic centers as the initial positions, are reported here unless otherwise noted. Example trace plots of select parameter chains to demonstrate good sampling behavior and convergence are shown in Fig. S4. Example posterior parameter distributions represented as histograms for the (x, y, z) fractional coordinated of one atom are shown in Fig. S5.

The 99% credible and prediction intervals resulting from the Bayesian refinement of the atomic positions with Model 1 (only Sn displacements allowed) are shown in Fig. 5a and with Model 2 (both Sn and Zr/Ti atomic displacements allowed) in Fig. 5b. The fit interval results for both models capture all the

observed superstructure reflection positions and are in good agreement with the intensities. The deviance information criteria (DIC) for both model results are reported in Table 3. The DIC is a Bayesian fit criteria, where lower values indicate a better model, that can be used to inform the relative fit quality of a model while also penalizing for overfitting [41]. Based on the DIC, Model 1 results in only a slightly better fit to the data as compared to Model 2.

The solved structures with the posterior parameter mean fractional atomic coordinates for both Model 1 and Model 2 are included in Supplemental Information as crystallographic information files. The solved Sn atomic positions from Model 1 are depicted as a crystal structure in Fig. 6a–d. The original nondisplaced positions are shown by the intersections of the guidelines for reference. The tin atoms displace in many directions at varying amplitudes, but there is a strong preference for displacement along the y-axis and z-axis ($[\overline{1}10]_c$ and $[001]_c$ directions of the parent cubic unit cell). Minimal displacement of the tin atoms is observed along the x-axis.

The solved Sn and Zr/Ti atomic positions from Model 2 are depicted as a crystal structure in Fig. 6e–h. The Zr/Ti atoms displace in all directions, but predominantly along the y- and z-axes ($[\overline{1}10]_c$ and $[001]_c$). The tin atoms also displace from their original positions in all directions, similar to the displacements observed in Model 1. In Model 2, however, the magnitude of

Figure 4 Comparison of the experimental, highresolution XRD pattern and the predicted pattern refined using the Rietveld method for the BSZT data modeled as two phases: BaZr_xTi_{1-x}O₃ and $SnZr_rTi_{1-r}O_3$. The range is zoomed in to better show the calculated pattern, though refinements were performed over a 2θ range of 2–45°. Phases are indicated with colored tick marks, including impurity phases, with the difference curve shown underneath.

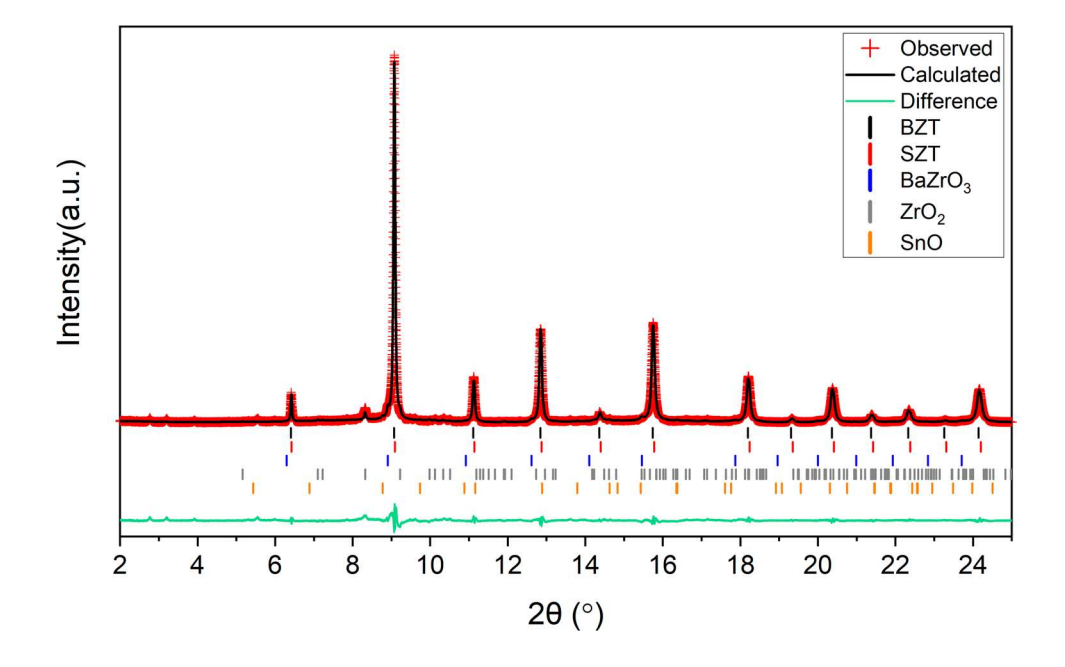
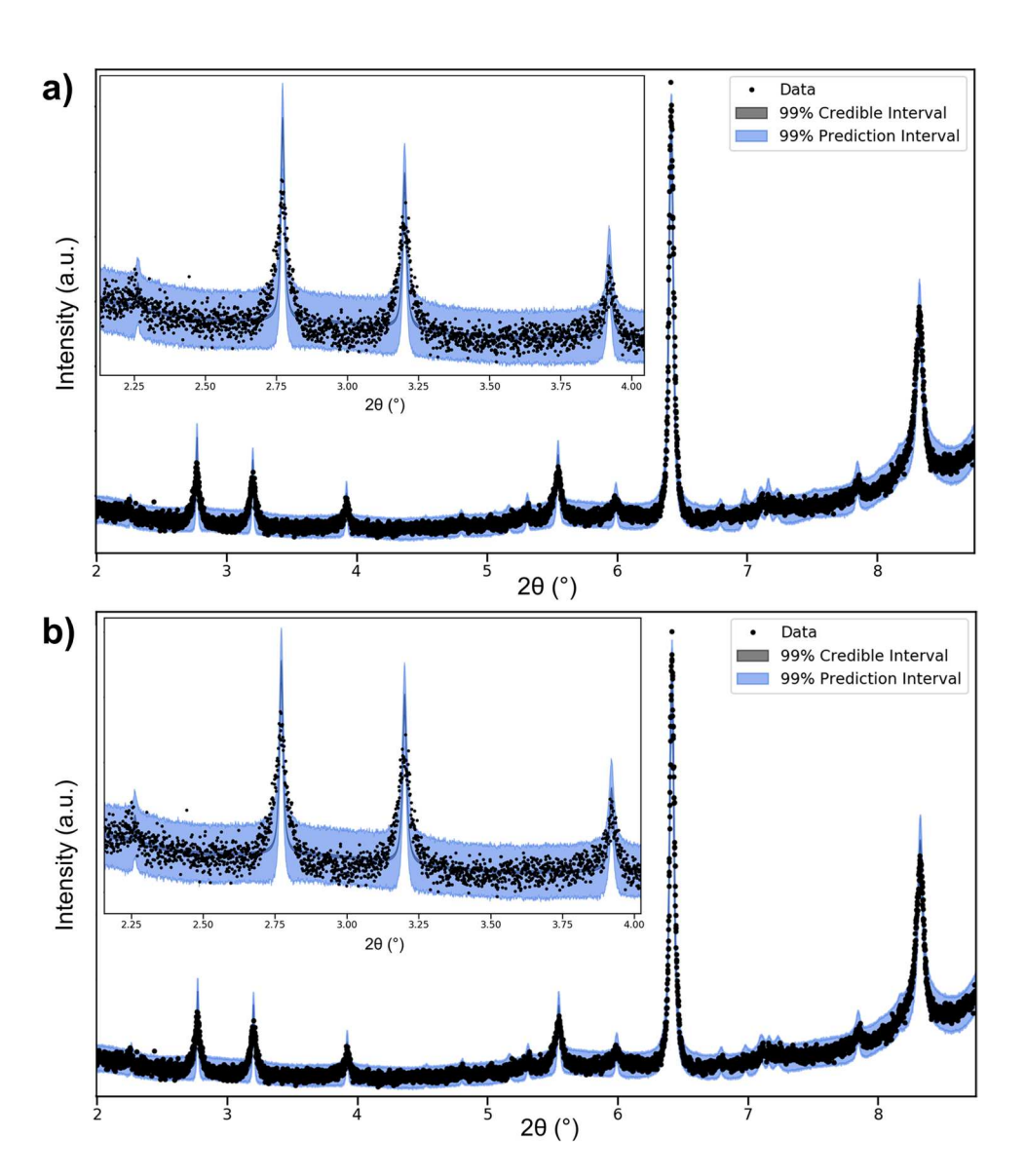




Figure 5 99% credible and prediction intervals showing model fit to data in the low 2θ range for a Sn displacement Model 1 and b Sn + Zr/ Ti displacement Model 2. The prediction intervals for both models cover that data well, match all the superstructure reflection positions, and roughly fit the intensities. Inset shows a zoomed in view of the first four peaks.



atomic displacements of the Sn A-site atoms is more pronounced than that of the Zr/Ti B-site atoms.

With the atomic positions of the SZT supercell determined using the Bayesian approach for Model 1 and Model 2, refinements with the Rietveld method using these supercells were performed. All supercell parameters were fixed at the Bayesian posterior mean parameter values while only histogram scale, microstrain, and background were refined. The resulting fit for the Model 1 supercell with only Sn displacements is plotted in Fig. 7. This model provides a good fit to the superstructure reflections in the low 2θ region, similar to the Bayesian model results. As 2θ increases beyond the limits set in the Bayesian approach, the model continues to be a reasonable fit to both the superstructure reflections and the main perovskite

reflections. The weighted pattern residual factors for refinements over two different 2θ ranges are listed in Table 3. Similar fit qualities are found for Model 1 and Model 2. In this context, neither model is deemed more suitable than the other and either displacing only the Sn or both the Sn and the Zr/Ti yields an adequate fit to the data. By utilizing the mean posterior atomic positions from the Bayesian method, a good fit was achieved for the observed superstructure reflections and a supercell was defined as a first step toward understanding the structure of the SZT compound.

Symmetry analysis

The Bayesian solution for atomic positions within a supercell provides information even with nearly no



h)

0

Sn

Zr/Ti

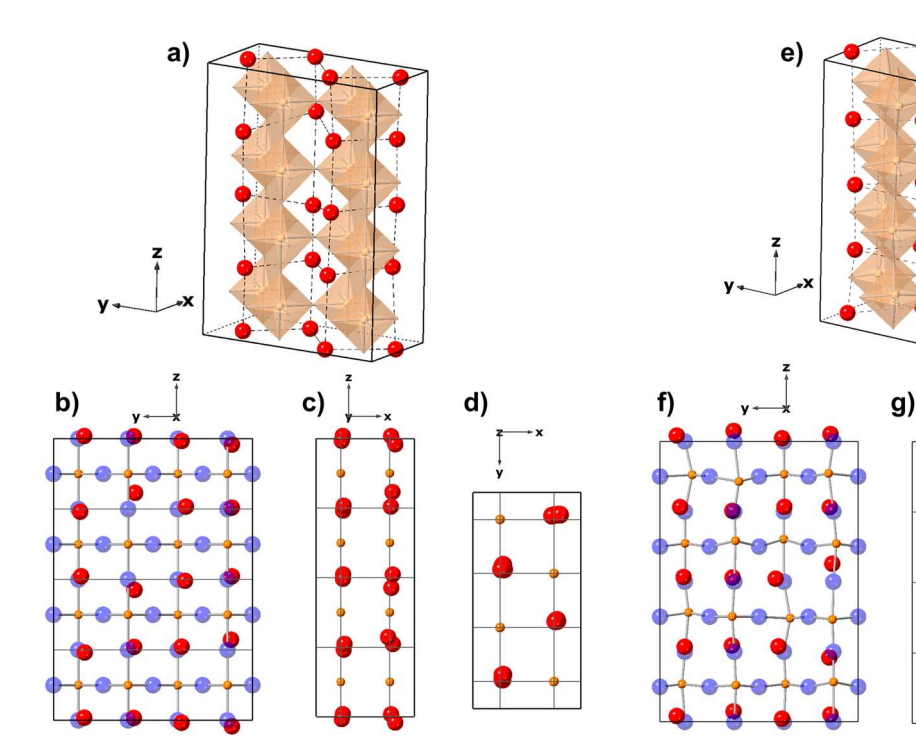


Figure 6 Visual representation of the solved supercell with atomic positions from the Bayesian method. Model 1 is displayed on the left $(\mathbf{a}-\mathbf{d})$ and Model 2 is displayed on the right $(\mathbf{e}-\mathbf{h})$. The full supercells (\mathbf{a}, \mathbf{e}) and projections along the (\mathbf{b}, \mathbf{f}) x-, (\mathbf{c}, \mathbf{g}) y-, and (\mathbf{d}, \mathbf{h}) z-axes are shown. Red atoms are the Sn atoms, orange atoms are the Zr/Ti atoms, orange polyhedra represent the oxygen

octahedra, and blue atoms are the fixed oxygen atoms. The dotted lines in (**a**, **e**) show the Sn–Sn atom distances. The intersections of the gray guidelines in (**c**, **d**, **g**, **h**) show the original nondisplaced atomic positions. All images were generated in Crystal Maker [40]

prior knowledge of the structure. This approach is useful for determining an initial, symmetry-less *P*1 structure definition. Although the displacements of the Sn and Zr/Ti atoms could appear to be predominantly random in all directions in the Bayesian supercell solution, a closer look provides more information about the symmetries within the structure and relationships between atoms. In this section, symmetry considerations of the solved supercell and an evaluation of the atomic displacements within the cell are discussed.

First, we consider the impacts of the oxygen octahedra on the observed superstructure reflections and the calculated pattern from the final structure definition. The effects of oxygen behaviors were not included in the supercell model. However, from the tolerance factor calculation and the behaviors expected in distorted perovskite structures, it is likely that the oxygen octahedra undergo tilting or other distortions in the tin-containing perovskite. To evaluate the consequences of omitting the oxygen distortions from this study, the oxygen positions of orthorhombic PbZrO₃ from Corker et al. [21], doubled along the *z*-axis, were

substituted into the Bayesian unit cell with Sn and Ti/Zr displacements. By comparing simulated patterns of the unit cell with tilted and non-tilted oxygen octahedra, it was found that distortions of the oxygen octahedra do not significantly impact the intensities of simulated XRD reflections at low 2θ (Fig. S6). Thus, it can be concluded that allowing the oxygen to displace in the model would not significantly impact the fit results.

With only powder X-ray diffraction information, the full symmetry of the unit cell including the oxygen octahedra behavior cannot be completed described. To do so, further information about the oxygen atoms would be necessary from other data collection methods, such as neutron or electron diffraction. Nonetheless, within the definitions of the SZT supercell focused on the A-site (i.e., Sn) and B-site (i.e., Zr/Ti) displacement behaviors obtained from the Bayesian approach, it may be possible to assign a higher symmetry space group than *P*1. The resulting supercell structures were analyzed in the program FINDSYM to identify possible space groups and symmetry



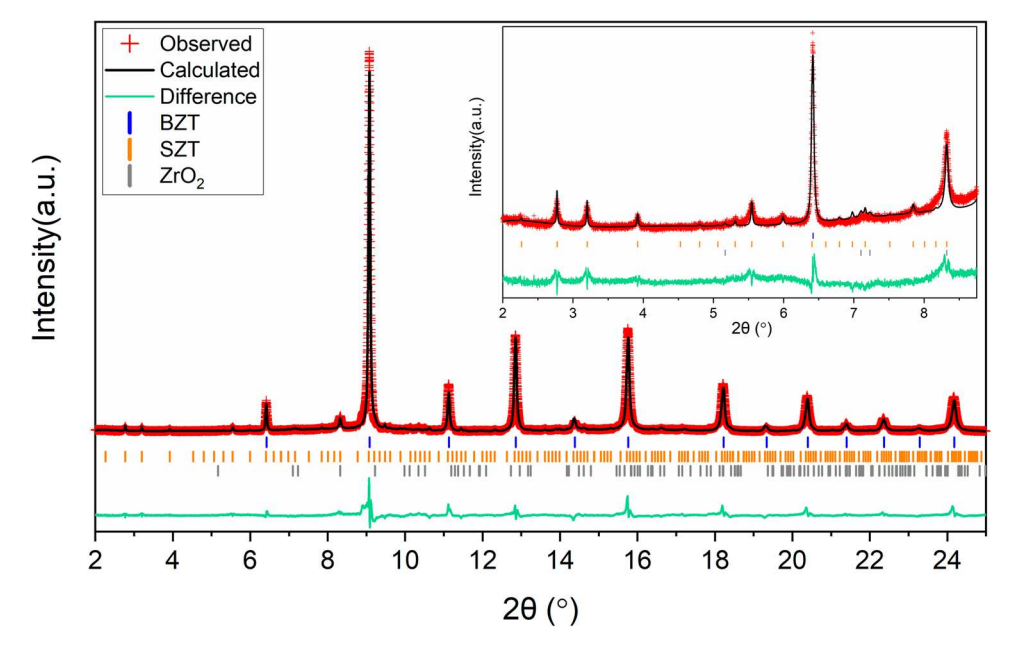
behaviors [42, 43]. The solved atomic positions from all three differently initialized Bayesian chains (to test for convergence of solutions) for both Model 1 and Model 2 were analyzed in the FINDSYM program. A unit cell with monoclinic space group of Pm and lattice parameters of a = 5.798 Å, b = 16.4 Å, and c = 11.596 Å within an atomic position tolerance of 0.5 Å and lattice parameter tolerance of 0.001 Å was identified for all three solved supercells of both Model 1 and Model 2. For an atomic position tolerance less than 0.3 Å, no symmetry was identified for any of the structure definitions. Crystallographic information files (cif) for the structure defined in the Pm setting for both Model 1 and Model 2 are included in the supplemental information.

Another technique that can help to understand the distortion behavior of the supercell structural solution is symmetry mode decomposition. Symmetry mode decomposition, also known as distortion mode analysis, is helpful in relating a high symmetry parent structure to a lower symmetry distorted structure through identifying symmetry-breaking distortion modes [44]. In this case, the parent structure is defined as the Pm3m cubic unit cell with atomic positions Sn(0,0, 0, Ti/Zr(0.5, 0.5, 0.5), O(0.5, 0.5, 0). The low symmetry structure is the supercell, with atomic positions defined by the Bayesian crystallographic refinement solution. An analysis of the symmetry modes with this cubic perovskite parent phase and the supercell distorted phase was performed and compared using both ISODISTORT and AMPLIMODES [44–47]. The

complete list of nonzero distortion modes in the supercell identified by the AMPLIMODES program is summarized in supplemental Table S2 for Model 1 and in Table S3 for Model 2. In this analysis, only the 'chain 1' solution for each model is presented as no significant differences were notable across the results with different parameter initializations. For Model 1, the largest identified distortion mode was Γ_4^- with an overall amplitude of 1.3346 Å and a normalized polarization vector defined in the low symmetry unit cell of (0.017, -0.019, 0.0039) on all Sn atoms in the supercell, which is shown in Fig. 8a-d. Other modes were found to have non-insignificant amplitude values, but only the Γ_{4}^{-} is addressed here as it is notably the largest, and thus primary, symmetry mode. For Model 2, the largest distortion mode identified was also Γ_{A}^{-} with an overall amplitude of 1.5381 Å and a normalized polarization vector defined in the low symmetry unit cell of (0.0075, 0.0098, 0.0119) on all Sn atoms and (-0.0055, -0.0038, 0.0050) on all Zr/Ti atoms in the supercell, displayed in Fig. 8e-h. Again, other modes were identified that have non-insignificant amplitude values, but only the Γ_{\perp} is addressed here as the largest and primary symmetry mode.

The order parameter corresponding with the Γ_4^- irrep is classified as ferroelectric for both models in ISODISTORT, indicating a proper ferroelectric as this is the primary order parameter. In Fig. 4d and h, the displacements of the Γ_4^- irrep are shown on the reduced unit cell transformed from the supercell back to the original cubic lattice setting. The displacement

Figure 7 Refinement results with the Rietveld method of BSZT data with tick marks indicating included phases of BZT, SZT Bayesian-solved supercell Model 1, and ZrO_2 impurity. The full pattern refined for a 2θ range from 2 to 25° is shown. The inset displays a zoomed-in view to highlight the superstructure reflections.





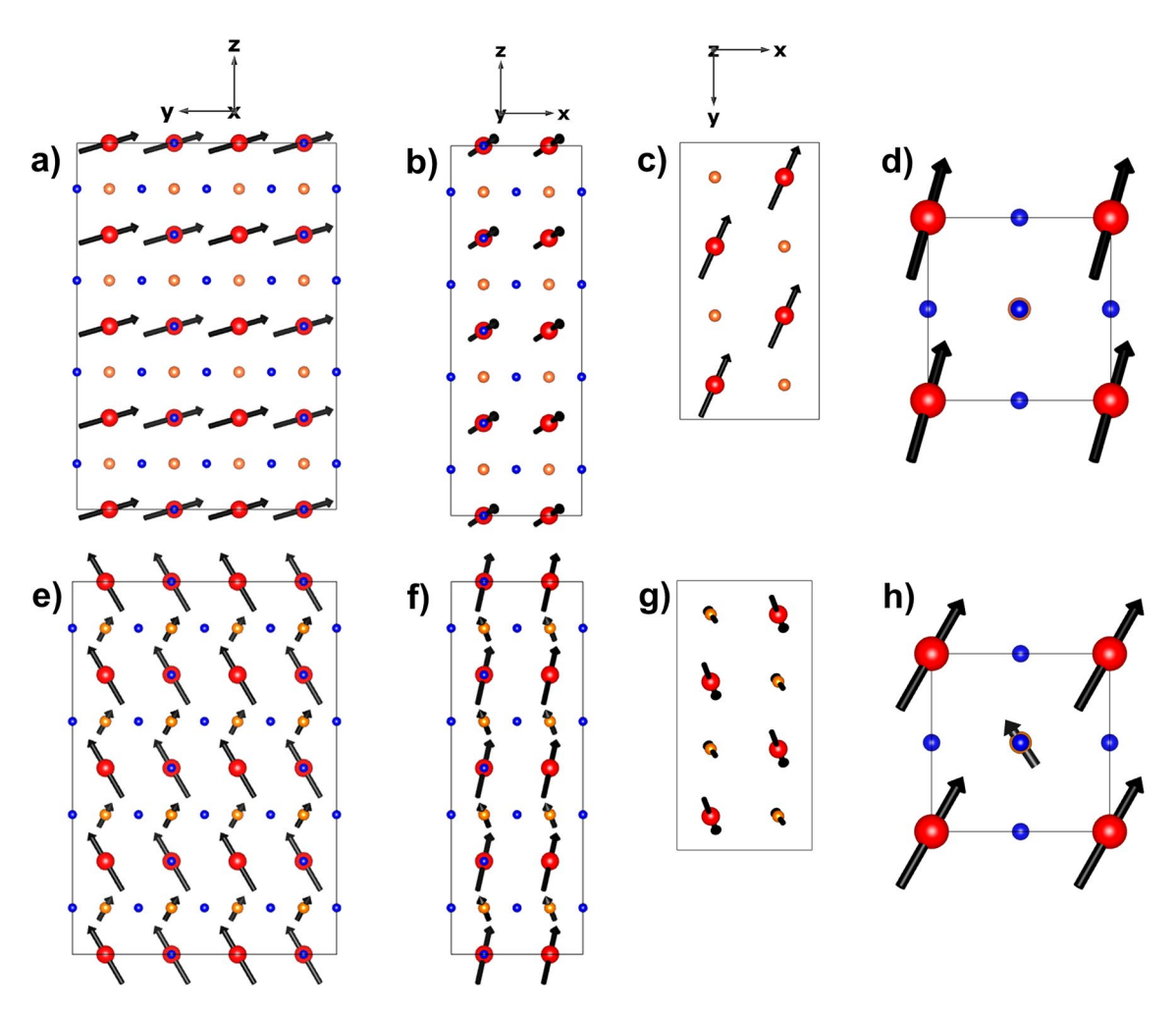


Figure 8 Atomic displacements of the Γ_4^- irrep mode represented as vectors on the corresponding atoms for $(\mathbf{a}-\mathbf{d})$ Model 1 and $(\mathbf{e}-\mathbf{h})$ Model 2. The displacements are shown along the (\mathbf{a}, \mathbf{e}) x-, (\mathbf{b}, \mathbf{f}) y-, and (\mathbf{c}, \mathbf{g}) z-axes of the supercell. The displacements of the supercells transformed back to the parent cubic lattice definition are compared for (\mathbf{d}) Model 1 and (\mathbf{h}) Model 2. The atomic

displacements are represented as black arrows, tin atoms as red spheres, the shared B-site Zr/Ti atoms as orange spheres, and the oxygen atoms as blue dots. The atomic radii are not to scale as the relative size of the oxygen atoms was reduced for better visibility of the displacement vectors.

vectors on the Sn atoms are fairly similar for Model 1 and Model 2, which suggests that the main contribution to the disruption of the original cubic cell is the incorporation of the Sn atoms into the lattice. The subsequent Sn distortions lead to the identified Γ_4^- primary mode, indicating the potential for ferroelectric distortion behavior in the SZT structure.

Conclusions

The crystal structure of metastable 40% Sn(II)-substituted BZT has been studied through the analysis of high-resolution synchrotron XRD and observation of decomposition with high-temperature XRD. The underlying cubic lattice of the precursor BZT is maintained throughout the tin substitution. The presence of superstructure peaks in the XRD pattern indicates that Sn(II) atoms are distorting within a supercell of the perovskite structure. Applying a novel Bayesian



refinement method enables all atomic displacements to simultaneously refine without getting caught in unreasonable solutions to determine the most probable configuration of atoms in the supercell. The Bayesian approach helps to overcome the challenges of structure determination from low-intensity superstructure peaks, overlapping reflections, and lacking known symmetry behavior, which is accomplished through the incorporation of prior information that constrains the allowable atomic positions and by applying sampling methods that make inferences conditional on the data. It is found that two models for atomic displacements can account for all of the superstructure reflections: a model with Sn²⁺ atoms displaced from their centrosymmetric positions within the cubic perovskite and a model with both Sn²⁺ and Zr⁴⁺/Ti⁴⁺ atoms displaced. These displacements disrupt the parent cubic unit cell symmetry and create a superstructure, which can be appropriately represented as a $\sqrt{2}a_c \times 4a_c \times 2\sqrt{2}a_c$ supercell with no symmetry constraints. The cation displacements found from the Bayesian solution can be modeled using a monoclinic Pm space group within a tolerance of 0.5 Å. Additionally, symmetry mode analysis reveals the possibility of a primary Γ_4^- ferroelectric distortion mode from the tin atoms. Ultimately, well-defined structural models enable the improvement in synthesis procedures and further the understanding of expected properties, specifically in regard to structural distortions.

Supplementary information

Supplementary information includes crystallographic information files for the $\rm SnZr_{0.5}Ti_{0.5}O_3$ P1 solved supercell and symmetry-analysis Pm supercell for Model 1 and Model 2. A pdf with supplemental figures and tables is also included to supplement the main text.

Acknowledgements

This material is based upon work supported by the National Science Foundation Graduate Research Fellowship Program under Grant No. DGE-1746939 and by the National Science Foundation under Grant No.

DMR-2004455. The Data-Enabled Science and Engineering of Atomic Structures (SEAS) program is gratefully acknowledged, including its members, including but not limited to Ralph Smith, Brian Reich, and Alyson Wilson. The SEAS program was supported by the National Science Foundation under Grant No. DGE-1633587. Any opinions, findings, and conclusions or recommendations expressed in this material are those of the author(s) and do not necessarily reflect the views of the National Science Foundation. Use of the Advanced Photon Source at Argonne National Laboratory was supported by the U.S. Department of Energy, Office of Science, Office of Basic Energy Sciences, under Contract No. DE-AC02-06CH11357.

Funding

The work was supported by the U.S. National Science Foundation under DGE-1746939, DMR-2004455, and DGE-1633587. Use of the Advanced Photon Source at Argonne National Laboratory was supported by the U.S. Department of Energy, Office of Science, Office of Basic Energy Sciences, under Contract No. DE-AC02-06CH11357.

Code availability

A version of the code used to implement the Bayesian method for crystallographic refinement is publicly available in the Quantitative Uncertainty Analysis for Diffraction (QUAD) repository on GitHub: https://doi.org/10.5281/zenodo.4474424, https://github.com/rabroughton/QUAD.

Declarations

Conflicts of interest The authors declare that there are no conflicts of interest that would influence this work.

Ethical Approval Not applicable.

Supplementary Information The online version contains supplementary material available at https://doi.org/10.1007/s10853-024-09878-w.



References

- [1] Panda PK (2009) Review: environmental friendly lead-free piezoelectric materials. J Mater Sci 44:5049–5062. https:// doi.org/10.1007/s10853-009-3643-0
- [2] Rödel J, Jo W, Seifert KTP et al (2009) Perspective on the development of lead-free piezoceramics. J Am Ceram Soc 92:1153–1177. https://doi.org/10.1111/j.1551-2916.2009. 03061.x
- [3] Uratani Y, Shishidou T, Oguchi T (2008) First-principles study of lead-free piezoelectric SnTiO₃. Jpn J Appl Phys 47:7735–7739. https://doi.org/10.1143/JJAP.47.7735
- [4] Ribeiro RAP, De Lazaro SR (2017) DFT/PBE0 study on structural, electronic and dielectric properties of SnZr_{0.5}Ti_{0.5}O₃ lead-free ferroelectric material. J Alloy Compd 714:553–559. https://doi.org/10.1016/j.jallcom. 2017.04.255
- [5] Pitike KC, Parker WD, Louis L, Nakhmanson SM (2015) First-principles studies of lone-pair-induced distortions in epitaxial phases of perovskite SnTiO₃ and PbTiO₃. Phys Rev B 91:035112. https://doi.org/10.1103/PhysRevB.91. 035112
- [6] Laurita G, Page K, Suzuki S, Seshadri R (2015) Average and local structure of the Pb-free ferroelectric perovskites (Sr, Sn)TiO₃ and (Ba, Ca, Sn)TiO₃. Phys Rev B 92:214109. https://doi.org/10.1103/PhysRevB.92.214109
- [7] Gardner J, Thakre A, Kumar A, Scott JF (2019) Tin titanate—the hunt for a new ferroelectric perovskite. Rep Prog Phys 82:092501. https://doi.org/10.1088/1361-6633/ ab37d4
- [8] O'Donnell S, Chung C-C, Carbone A et al (2020) Pushing the limits of metastability in semiconducting perovskite oxides for visible-light-driven water oxidation. Chem Mater 32:3054–3064. https://doi.org/10.1021/acs.chemmater.0c00044
- [9] Gabilondo EA, O'Donnell S, Broughton R et al (2021) Synthesis and stability of Sn(II)-containing perovskites: (Ba,Sn^{II})Hf^{IV}O₃ versus (Ba,Sn^{II})Sn^{IV}O₃. J Solid State Chem 302:122419. https://doi.org/10.1016/j.jssc.2021.122419
- [10] Gabilondo EA, Newell RJ, Chestnut J et al (2022) Circumventing thermodynamics to synthesize highly metastable perovskites: nano eggshells of SnHfO₃. Nanoscale Adv 4:5320–5329. https://doi.org/10.1039/D2NA00603K
- [11] Reaney IM, Woodward DI, Randall CA (2011) Displacive phase transitions and intermediate structures in perovskites. J Am Ceram Soc 94:2242–2247. https://doi.org/10. 1111/j.1551-2916.2010.04377.x
- [12] Glazer AM (1975) Simple ways of determining perovskite structures. Acta Cryst A 31:756–762. https://doi.org/10. 1107/S0567739475001635

- [13] Woodward DI, Reaney IM (2005) Electron diffraction of tilted perovskites. Acta Crystallogr B Struct Sci 61:387– 399. https://doi.org/10.1107/S0108768105015521
- [14] Singh SP, Paterson AR, Wendelberger LJ, et al (2020) Algorithms in Diffraction Profile Analysis. In: Kalidindi S, Kalinin SV, Lookman T (eds) Handbook on big data and machine learning in the physical sciences. World Scientific, Singapore, pp 501–539. https://doi.org/10.1142/ 9789811204555_0015
- [15] Fancher CM, Han Z, Levin I et al (2016) Use of Bayesian inference in crystallographic structure refinement via full diffraction profile analysis. Sci Rep 6:31625. https://doi.org/10.1038/srep31625
- [16] O'Donnell S, Osborn DJ, Krishnan G et al (2022) Prediction and kinetic stabilization of Sn(II)-perovskite oxide nanoshells. Chem Mater 34:8054–8064. https://doi.org/10.1021/acs.chemmater.2c02192
- [17] Toby BH, Von Dreele RB (2013) GSAS-II: the genesis of a modern open-source all purpose crystallography software package. J Appl Crystallogr 46:544–549. https://doi.org/ 10.1107/S0021889813003531
- [18] Degen T, Sadki M, Bron E et al (2014) The HighScore suite. Powder Diffr 29:S13–S18. https://doi.org/10.1017/ S0885715614000840
- [19] rabroughton (2021) Quantitative Uncertainty Analysis of Diffraction (QUAD), https://doi.org/10.5281/zenodo.44744 24, https://github.com/rabroughton/QUAD
- [20] Smith RC (2013) Uncertainty quantification: theory, implementation, and applications. Society for Industrial and Applied Mathematics, Philadelphia
- [21] Corker DL, Glazer AM, Dec J et al (1997) A Re-investigation of the crystal structure of the perovskite PbZrO₃ by X-ray and neutron diffraction. Acta Cryst B 53:135–142. https://doi.org/10.1107/S0108768196012414
- [22] Glazer AM, Roleder K, Dec J (1993) Structure and disorder in single-crystal lead zirconate, PbZrO₃. Acta Cryst B 49:846–852. https://doi.org/10.1107/S0108768193005129
- [23] Soejima Y, Yamasaki K, Fischer KF (1997) Use of X-ray anomalous dispersion: the superstructure of PbZrO₃. Acta Cryst B 53:415–419. https://doi.org/10.1107/S010876819 7002759
- [24] Yamasaki K, Soejima Y, Fischer KF (1998) Superstructure determination of PbZrO₃. Acta Crystallogr B Struct Sci 54:524–530. https://doi.org/10.1107/S0108768197018466
- [25] Sawaguchi E, Maniwa H, Hoshino S (1951) Antiferroelectric structure of lead zirconate. Phys Rev 83:1078–1078. https://doi.org/10.1103/PhysRev.83.1078
- [26] Karimi S, Reaney IM, Levin I, Sterianou I (2009) Nd-doped BiFeO₃ ceramics with antipolar order. Appl Phys Lett 94:112903. https://doi.org/10.1063/1.3097222



- [27] Levin I, Tucker MG, Wu H et al (2011) Displacive phase transitions and magnetic structures in Nd-substituted BiFeO₃. Chem Mater 23:2166–2175. https://doi.org/10.1021/cm1036925
- [28] Levin I, Karimi S, Provenzano V, et al (2010) Reorientation of magnetic dipoles at the antiferroelectric-paraelectric phase transition of $\text{Bi}_{1-x}\text{Nd}_x\text{FeO}_3$ (0.15 \leq x \leq 0.25). Phys Rev B 81:020103. https://doi.org/10.1103/PhysRevB.81.020103
- [29] Sakowski-Cowley AC, Łukaszewicz K, Megaw HD (1969) The structure of sodium niobate at room temperature, and the problem of reliability in pseudosymmetric structures. Acta Crystallogr B Struct Sci 25:851–865. https://doi.org/ 10.1107/S0567740869003141
- [30] Hewat AW (1974) Neutron powder profile refinement of ferroelectric and antiferroelectric crystal structures: Sodium niobate at 22°C. Ferroelectrics 7:83–85. https:// doi.org/10.1080/00150197408237955
- [31] Khalyavin DD, Salak AN, Olekhnovich NM et al (2014) Polar and antipolar polymorphs of metastable perovskite BiFe_{0.5}Sc_{0.5}O₃. Phys Rev B 89:174414. https://doi.org/10. 1103/PhysRevB.89.174414
- [32] Khalyavin DD, Salak AN, Fertman EL et al (2019) The phenomenon of conversion polymorphism in Bi-containing metastable perovskites. Chem Commun 55:4683–4686. https://doi.org/10.1039/C9CC00472F
- [33] Campo CM, Rodríguez JE, Ramírez AE (2016) Thermal behaviour of romarchite phase SnO in different atmospheres: a hypothesis about the phase transformation. Heliyon 2:e00112. https://doi.org/10.1016/j.heliyon.2016. e00112
- [34] Shannon RD (1976) Revised effective ionic radii and systematic studies of interatomic distances in halides and chalcogenides. Acta Cryst A 32:751–767. https://doi.org/10.1107/S0567739476001551
- [35] http://abulafia.mt.ic.ac.uk/shannon/ptable.php
- [36] Sidey V (2022) On the effective ionic radii for the tin(II) cation. J Phys Chem Solids 171:110992. https://doi.org/10. 1016/j.jpcs.2022.110992
- [37] Harris KDM, Tremayne M, Kariuki BM (2001) Contemporary advances in the use of powder X-ray diffraction for structure determination. Angew Chem Int Ed 40:1626–1651. https://doi.org/10.1002/1521-3773(20010504)40:9%3c1626::AID-ANIE16260%3e3.0.CO:2-7
- [38] Altomare A, Cuocci C, Giacovazzo C et al (2013) EXPO2013: a kit of tools for phasing crystal structures

- from powder data. J Appl Crystallogr 46:1231–1235. https://doi.org/10.1107/S0021889813013113
- [39] Gabilondo EA, Newell RJ, Broughton R, et al (2023) Switching lead for tin in PbHfO₃: noncubic structure of SnHfO₃. Angew Chem Int Ed, e202312130. https://doi.org/ 10.1002/anie.202312130
- [40] Structure and images generated using CrystalMaker®: a crystal and molecular structures program for Mac and Windows. CrystalMaker Software Ltd, Oxford, England. www. crystalmaker.com
- [41] Reich BJ, Ghosh SK (2019) Bayesian statistical methods. CRC Press, Taylor & Francis Group, Boca Raton
- [42] Stokes HT, Hatch DM (2005) FINDSYM: program for identifying the space-group symmetry of a crystal. J Appl Crystallogr 38:237–238. https://doi.org/10.1107/S0021 889804031528
- [43] Stokes HT, Hatch DM, Campbell BJ (2023) FINDSYM, v. 7.1.6, ISOTROPY Software Suite, iso.byu.edu
- [44] Perez-Mato JM, Orobengoa D, Aroyo MI (2010) Mode crystallography of distorted structures. Acta Crystallogr A Found Crystallogr 66:558–590. https://doi.org/10.1107/ S0108767310016247
- [45] Stokes HT, Hatch DM, Campbell BJ (2023) ISODISTORT, v. 6.12.1, ISOTROPY Software Suite, iso.byu.edu
- [46] Campbell BJ, Stokes HT, Tanner DE, Hatch DM (2006) ISODISPLACE: a web-based tool for exploring structural distortions. J Appl Crystallogr 39:607–614. https://doi.org/ 10.1107/S0021889806014075
- [47] Orobengoa D, Capillas C, Aroyo MI, Perez-Mato JM (2009) AMPLIMODES: symmetry-mode analysis on the Bilbao Crystallographic Server. J Appl Crystallogr 42:820– 833. https://doi.org/10.1107/S0021889809028064

Publisher's Note Springer Nature remains neutral with regard to jurisdictional claims in published maps and institutional affiliations.

Springer Nature or its licensor (e.g. a society or other partner) holds exclusive rights to this article under a publishing agreement with the author(s) or other rightsholder(s); author self-archiving of the accepted manuscript version of this article is solely governed by the terms of such publishing agreement and applicable law.

